Microstructure and activation volume of a Cu-6 wt %Zn brass processed by equal channel angular pressing

Amina Turki, Bruno Guelorget, Virgil Optasanu, Manuel François, Frédéric Herbst, Nabil Njah

This is a working version; the final article can be found here: https://doi.org/10.1016/j.jallcom.2023.171974

Microstructure and activation volume of Cu-6wt%Zn brass processed by equal channel angular pressing

Amina Turki[1], Bruno Guelorget[2], Virgil Optasanu[3], Manuel François[2], Frédéric Herbst[3], Nabil Njah[1]*

[1]GEOGLOB Lab, Materials Group, Sfax Faculty of Sciences, University of Sfax, PB 1171, 3000 Sfax, Tunisia

[2]Université de technologie de Troyes, UR LASMIS, 12 rue Marie Curie - CS 42060 F-10004 Troyes Cedex

[3] ICB, UMR 6303 CNRS, Université de Bourgogne Franche Comté, 9 av. Alain Savary, 21078 Dijon Cedex, France

Abstract

The generation of a high density of twins few tens nanometers in size can enhance both strength and ductility. The present work aims to produce highly twinned microstructure in Cu-6wt% Zn alloy of a moderate stacking fault energy (SFE) by equal channel angular pressing (ECAP) using a die with angles ϕ=110° and Ψ=0. X ray diffraction (XRD) shows that a high density of defects is stored up to 2 passes then a recovery takes place. EBSD imaging reveals a high density of twins and a fibrous microstructure. Grains close to 100nm in size are formed. Strain rate sensitivity (SRS) was investigated in compression and nanoindentation (NI). Compression curves show that deformation occurs by slipping with a contribution of twins to hardening. A high contribution of shear bands was revealed during ECAP and compression tests. The activation volume V* in compression and NI is in the range $70b^3$ - $100b^3$, consistent with the emission of dislocations from grain boundaries and twin boundaries The experimental values of V* were compared to those expected from defect densities.

Key words

Cu-Zn alloys; Microstructure; Compression; Nanoindentation; Strain rate sensitivity.

Highlights

- CuZn6 brass processed by ECAP was characterized by XRD, EBSD, compression and nanoindentation (NI) tests
- Shear banding occurs in ECAP and continues in compression tests
- High twin density and grains close to 100 nm were created by ECAP.
- SRS values are comparable in compression and nanoindentation.
- Activation volumes are consistent with the regime of dislocation emission from grain boundaries.

1. Introduction

The combination of a high strength and a sufficient ductility is an important research issue in structural materials. However, a high strength is usually accompanied by a loss of ductility [1-3]. It has been reported that increasing the density of grain boundaries (GBs) or twin boundaries (TBs) can lead to a high strength without loss in ductility; this is because GB and TB impede dislocation slip as strong barriers and act at the same time as dislocation sources [2,4]. The saturation grain size (GSs), i.e. the minimum grain size (GS) achieved, tends to be leveled by the refinement process chosen among other severe plastic deformation (SPD), electrodeposition, vapor deposition. The deformation mechanisms play an important role on the GSs and the latter depends on whether slipping or twinning dominates. When slipping is dominant, GSs depends on the dislocation mobility and so, on their interaction with barriers such as forest dislocations, solute atoms, precipitates and GBs. Many parameters, such as stacking fault energy (SFE), influence this feature [5]. It has been shown in CuZn and CuAl alloys,

that decreasing the SFE by increasing the solute concentration reduces the GSs [6-9]. Thus, Mohamed [10] has proposed a formula relating the SFE to the GSs in ball milled nanocrystalline (nc) metals: $d_{min}/b = A(\gamma/Gb)^q$ where A and q are constants, G the shear modulus, b the magnitude of the Burgers vector of dislocations and γ the SFE . Furthermore, it has been suggested that the exponent q is higher when refinement occurs by twinning or by shear banding [11-13]. Bruder et al. [5] suggest that GSs is controlled by dislocation annihilation rate, itself controlled by the dislocation dissipation within GB rather than by their incorporation in GB. Wu et al. [14] proposed a mechanism of grain formation by twin reactions. They suggest that the grains become finer if the deformation occurs by twinning rather than by slipping. Moreover, deformation by twinning is an important feature since it leads to high hardening rate [15,16]. Coarse grained materials become difficult to deform by twinning when GS is reduced whereas in nc materials the opposite trend is remarked [17-19]. The formation of grains few tens of nanometers in size within twin lamella has been frequently reported; this was related to a twin fragmentation into micro- and nano-twins [9,12,20,21]. The thinner the lamella, the smaller the GS. Therefore, the generation of nano-twins has taken a great importance. In nc FCC materials, twins nucleate mostly by the emission of 1/6 <112> partial dislocations from GB [17,22]; this was proved by molecular dynamic (MD) simulation [18] and verified by HRTEM observations [22]. Thus, in nickel of ∼25nm grains, twinning was observed after deformation in liquid Nitrogen despite of the high SFE [17,23]; this was explained by the nucleation of partials 1/6 <112> at twin boundaries (TBs) that do not behave as those from dissociation of perfect dislocations [24]. The critical GS that enables partial emission depends on the SFE and, to a lesser extent, on the deformation procedure [17,25,26].

In many cases, deformation leads also to twins fragmentation (de-twinning) [27-33]; the mechanism is less investigated even though de-twinning caused by shear banding was reported in alloys deformed at very high strain rates [30].

Among the various mechanical characterizations of alloys, the ones giving access to the kinetic and thermodynamic characteristics of deformation are of great importance. The SRS parameter *m* and the related activation volume *V** are two important parameters [34,35]. The activation volume *V** is the number of atoms that have to be coherently thermally activated to move the dislocations over localized obstacles in their slip planes [36], or the area swept by the dislocations during the thermal activation process times the Burgers vector of the dislocations. It is generally reported that small *V** values ($\approx 20b^3$)are expected if GB sliding is the main mechanism of deformation which operates at low stresses. In contrast, high V* values ($\geq 100b^3$)at higher stresses indicate an important contribution of dislocations.

ECAP is widely used as a mechanical process of grain refinement; it has the advantage of creating a high amount of deformation without changes in specimen shape. Since its introduction, it has undergone several modifications to be applied to sheets [37] or to be repeated several times without the sample leaving the die by using a rotary-die [38,39]. Copper–Zinc (Cu-Zn) brasses are of considerable interest for studying the deformation mechanisms whenever SFE is involved; their good castability allows preparing massive ingots with the possibility of controlling SFE through the zinc content.

The aim of the present work is to study the microstructure and the mechanical behavior of a fine grained Cu - 6wt% Zn alloy processed by ECAP. Electron Backscatter Diffraction (EBSD) imaging and X-ray diffraction (XRD) were used to characterize the microstructure in term of grain size and defect density. Compression tests were performed to check the slipping/twinning mechanisms of deformation. The SRS and V* were evaluated from nanoindentation and compression tests. The results of the two methods are compared and discussed.

2. Material and methods

The alloy Cu-Zn6 was prepared by melting together weighed quantities of Cu a1 copper and Cu-38Zn-2Pb (wt%) in a crucible furnace using the steering melting procedure and casting in a sand mold. The alloy was then homogenized for 24 hours at 600°C and quenched in iced water. The chemical and phase alloy composition were verified X-ray fluorescence (XRF) and XRD. XRF analysis leads to a Zn content of (5.8$\pm$0.3) wt%. From the lattice parameter obtained by XRD and using the empirical expression of the lattice constant: $a_{CuZn} = a_{Cu} + 2.359\ 10^{-4} \times (wt\%Zn)$[40] where a_{Cu}= 0.3610 nm and a_{CuZn} = 0.3625 nm; this leads to a zinc content of 6.3wt%. Pb content is less than 0.2wt% as was obtained from XRF. The corresponding SFE is 24 mJ/m^2 as was obtained from a linear interpolation of the values given by El Danaf et al. [41] as a function of composition. Specimens for ECAP 70 mm in length and 11 mm in diameter were prepared by wire cut electrical discharge machining. ECAP was performed using a hydraulic press under a pressure of ~300 MPa at a rate of 5 mm/min. The die was machined from tool steel; the characteristic angles are Φ = 110° and Ψ = 0° [42]; this leads to an equivalent strain of ε_N = 0.7N where N is the number of passes [43]. Before each pass, the specimens were coated with a lubricant containing colloidal MoS_2 suspension.

EBSD, XRD and NI investigations were performed on the cross-section of the extruded specimens i.e. on X plane [44]. Specimens for EBSD were mechanically polished up to 1 µm diamond powder suspension and then super-finished with 30 nm colloidal silica suspension with vibrant polishing. The EBSD observations were performed using a JEOL JSM 7600F SE microscope equipped with the EBSD TSL EDAX OIM system. The step size is generally recommended to be of the same order as the microstructure scale [45]; the steps used presently are 1 µm and 100nm for large and close-up images respectively. The grains were analyzed directly from the OIM images using pixel-to-pixel measurements. The GB exceeding a misorientation angle of 15° are considered as high-

angle grain boundaries (HAGBs). The KAM distribution was computed to obtain the density of the geometrically necessary dislocations ρ_{GND} by using the equation:

$$\rho_{GND} = \frac{\alpha.KAM}{b.R} \qquad (4)$$

where α is a constant which depends on the nature of dislocations edge or screw, a value α = 3 was adopted [46], b is the magnitude of the Burgers vector of dislocations. The KAM values are given by the EBSD software and R is the kernel size that takes into account the neighbor order considered in the KAM mapping. For a step size of 1 µm, R = 1 µm for the first neighbor, 3 µm for the third.

Compression tests were performed along the ECAP direction using a universal compression/tensile machine Tinius Olsen 50 KS piloted with Qmat software. Compared to tensile tests, compression ones provide higher strain with no failure but they do not give a direct information on the ductility. The specimens are 5.5 – 6 mm in height and 5 mm in diameter; they were machined by the same technique as the ECAP specimens (Fig.1). The machine stiffness was first measured by recording the force-displacement curve during platen to platen contact experiment. To reduce friction effect, the specimen surfaces in contact with the plates were coated with a lubricant containing colloidal MoS_2 suspension. True stress and true strain are defined by $\sigma = F/S$ and $\varepsilon = -\mathrm{Ln}(L/L_0)$ where F is the load, S, Lo and L are the instantaneous cross-section, the initial height and the instantaneous height of the specimen respectively. The initial strain rate is defined by $\dot{\varepsilon} = -\frac{1}{Lo}\left|\frac{dL}{dt}\right|$ and ranged between 3.10^{-4} and 30.10^{-4} s^{-1}. The stain rate sensitivity (SRS) parameter is defined by:

$$m = \left(\frac{\partial Ln\sigma}{\partial Ln\dot{\varepsilon}}\right) \qquad (1)$$

To check an eventual similarity of the deformation mechanisms, the SRS in nanoindentation (NI) was investigated for N=3 using the strain rate jump (SRJ) method [47,48] in continuous stiffness measurement (CSM). It is frequently observed in experiments with a Berkovich indenter, that the measured hardness H decreases with

increasing indentation depth; this is known as the indentation size effect (ISE) which makes difficult an accurate estimation of the bulk hardness. In the Nix-Gao model which considers an important effect of the GND dislocations, the measured hardness during CSM is depth dependent [49]:

$$H = Ho\sqrt{1+\frac{h^*}{h}} \qquad (2)$$

where H is the measured hardness, Ho the bulk hardness, h the indentation depth and h* the characteristic length scale of the indentation size effect (ISE).

The strain rate in NI experiments is defined by $\dot{\varepsilon} = \frac{1}{h}\left|\frac{dh}{dt}\right|$ and the SRS parameter by $m = \left(\frac{\partial LnHo}{\partial Ln\dot{\varepsilon}}\right)$; it is derived from the equation $\sigma = K\dot{\varepsilon}^m$ where σ is the flow stress and *K* is a material constant and from the linear relation linking Ho and σ.

NI tests were performed using a FT-NMT04 nanoindenter (FemtoTools) in a TESCAN MIRA4 SEM and a Berkovich tip. During a SRJ test, the loading rate is controlled to keep the strain rate constant at different predefined values. The strain rates were set to 0.001, 0.01, 0.1s^{-1}. Three tests were performed to get some statistics on the SRS parameter value m. In the CSM mode, the tip is oscillated at very low amplitudes when it is displaced. Because of these high-frequency oscillations (≈200Hz), the eventual retarded displacements (viscoelastic for example) are suppressed.

An estimation of the activation volume V* was performed by considering the concentration of the various obstacles for dislocations after ECAP. X ray diffraction (XRD) was used to calculate the defect concentrations after ECAP. In XRD, peak position and shape are differently influenced by the various defects [50,51]. In the present study, XRD experiments were focused on the calculations of the crystallite size D, the root mean square (rms) strain $\varepsilon_{rms} = \sqrt{\frac{2}{\pi}\frac{\Delta d}{do}}$ where Δd = d-do is the difference between the interplanar distances before and after deformation, and the twin density β. XRD patterns were recorded on the X planes at room temperature with a Philips X'Pert

system working at 40 kV in the theta/theta mode using Cu (Kα) radiation. The step size was 0.02° in theta and the counting time was 3 s/step. D and ε_{rms} were calculated from the breadth of the diffraction peaks using the Williamson-Hall (WH) method [52]. The $k\alpha_2$ component of each peak was first substracted using the X'Pert software. The instrumental broadening at a given angle θ was estimated from the NaCl spectrum and substracted from the experimental one. Twin faults are responsible for the peak shift, broadening and asymmetry in the XRD pattern [50]. The twin density β represents the probability of finding a twin fault between two neighboring (hkl) layers [50,53]; it was calculated using the formula [54, 55]:

$$\beta = \frac{\Delta(2\theta)_{111} - \Delta(2\theta)_{200}}{11\ tan\ \theta_{111} + 14.6\ tan\theta_{200}} \qquad (3)$$

where $\Delta(2\theta)_{hkl}$ represents the deviation of the center of gravity of each (hkl) peak from its maximum position.

3. Results

The Inverse pole figures (IPF) of the alloy before (N=0) and after ECAP for N = 3 are given in Fig. 2. In the initial state, the microstructure over the explored area consists of well-defined equiaxe grains of random orientations with many annealing twins. After ECAP for N=3, the orientations are randomly distributed with a tendency to alignment along a preferential direction. In Fig. 3 are given the Unique Grain Color (UGC), the Image Quality (IQ), and the Kernel Average Misorientation (KAM) images for N=3 recorded at a step size of 1 µm. IQ image shows a high density of deformation twins (examples are arrowed). Fig. 3c represents the KAM image by considering the misorientation between a referential pixel and its first neighbor. The color codes depict the dislocation density ρ_{GND} as calculated using equation (4). The mean dislocation density over the explored area was calculated to be 5.5 10^{14} m^{-2}.

The determination of the twin density β together with the stacking fault probability in nanocrystalline metals reveals many difficulties. In fact, due to the finite size, one crystallite should be faulted in only one crystallographic direction; for example in (111) for ones and $(\bar{1}11)$ for others [56]. As the position and the profile (breadth, asymmetry) of a given reflection (hkl) result from many contributions (components) regardless the sign and the order of h, k, l, the profiles of these contributions should be calculated separately and the resultant profile is made up by a summation [56]. The output parameters are then obtained by a superposition of calculated and experimental peaks. It is worth noting that all models assume a low density of defects. Nevertheless, equation (4) is still widely used [57,58].

XRD spectra of the alloy for N=0 and N=3 are plotted in Fig. 4a with a magnification of the peaks (111) and (200) of the FCC lattice. We note that the whole profiles of diffraction peaks are strongly modified after ECAP. Fig. 4b shows the evolution as a function of N, of the twin density β, the crystallite size D, the rms strain ε_{rms} and the dislocation density ρ. The latter was calculated using the equation [59]

$$\rho = \frac{2\sqrt{3}\varepsilon_{rms}}{D.b} \qquad (5)$$

The straining effects i.e. the increase of β, ε_{rms}, ρ and the decrease of D is remarked up to N = 2. For N = 3 a tendency to recovery is observed (Fig. 4). It is worth recalling that the dislocation density can be calculated among others, from the KAM and XRD. We have shown in previous work [60] that a good agreement is generally obtained between the two methods and that the difference arises from the sensitivity of the two techniques to the surface effect: X rays have a deeper penetration whereas EBSD is more sensitive to surface preparation.

Fig. 5 represents the stress-strain curves in compression recorded at different strain rates for different numbers of passes. To reveal whether deformation occurs by

twinning or by slipping, the curves of the normalized hardening rate $\theta = \frac{1}{\sigma}\frac{d\sigma}{d\varepsilon}$ were also plotted. An important increase in the flow stress is observed after ECAP. It is worth noting that during the tests, all the compression specimens keep a cylindrical shape and no barrel effect is observed; this reveals that deformation was roughly homogeneous over the specimen. Excepting for N = 0, the curves show a strain rate dependence of the 0.2% flow stress. Fig. 6 shows the hardness-depth curve of the alloy for N=3 in the CSM mode with several SR jumps. As it is often observed, the overall curve shows that the hardness decreases with depth then it remains nearly constant. In fact, from equation (2), reducing ISE requires high indentation depths where h*/h<<1.

4. Discussion

4.1. Microstructure

The IPF depicts the distribution of (hkl) planes over the specimens with the three reference orientations. For N=3, Fig. 2b shows various orientations that do not correspond necessarily to different grains but rather to various twinned regions. The generated twins in dark blue, are colored differently from the parent grain. The IQ image of Fig. 3b shows a high density of twins. On the other hand, the UGC image shows the formation of fine grains. Furthermore, referring to the color code used for the KAM cartography, the corresponding GND dislocation density and the corresponding unique grain color UGC map (Fig. 3a), the fine-grained region (arrowed) is almost free from dislocations as compared to the other regions. A general observation is that the new grains are located in twins and that the latter nucleate at GB; this feature is shown in Fig. 7 which is a magnification of the selected region of Fig. 3 a, b (white arrows). The region pointed by black arrows contains a high density of twins coated with fine grains. The fine-grained zones correspond usually to low IQ. In fact, since the IQ is a measure of the spread in diffracted intensity, the low values (dark gray) associated are due to the high density of GBs and other defects. Primary twins are occasionally fractioned by

secondary ones and the extent of twinning depends on the grain orientation: The red grain marked in Fig. 7a having the (001) plane normal to the ECAP direction is prone to slip and contains shear bands (Fig. 7b). The twinned grains colored in pink (referring to color key in Fig. 2a) are close to <112> and <111> directions which are favorable for twinning. Different mechanisms of twin formation are summarized in a review by Zhu et al. [17]. Among others, twin formation by emission of partial dislocations from GB was first predicted by molecular dynamic (MD) simulation [18] and then verified by HRTEM [61-63]; This means that the GB nucleation of twins occurs also in large grains. It is worth noting that in EBSD imaging, the resolution is limited by the step chosen so in this case, grains below 1 µm are not resolved. Fig.8 represents the microstructure of the alloy recorded at a step size of 100 nm. IQ image of Fig. 8a shows clear fibrous structure of the α phase (dark zones, arrowed) resulting from the creation of shear bands (SB). This trend, i.e. shear bands, is favored in alloys of medium and low SFE in which deformation twinning occurs extensively [9,64,65]; many twins are arrowed on the IPF (Fig. 8b). Furthermore, in FCC metals, deformation twinning generates a layered structure of fine and alternating twin-matrix (T-M) layers [9]. IPF and UGC images show a high density of fine grains 100-200nm in sizes coating these bands (Fig. 8b, c). Furthermore, in view of the limited resolution at the step size of 100 nm, the extent of refinement is not clearly revealed so that grains and twins below this size can be present. Deformation by shear bands has been observed in Cu-Al alloys single crystals and it was marked, on the compression curves, by sharp stress relaxations by mechanical twinning [66].

4.2. Compression behavior

The normalized hardening rate curves of the compression tests (Fig. 5) show a clear difference between the behavior before and after ECAP. For N=0, a progressive decrease of θ with a moderate slope is remarked showing that slipping is the main operating mechanism; this indicates that the required stress for twinning was not reached because of the low solid solution effect of Zn. The shape of the curves is then

the result of the traditional competition between strain hardening and dynamic recovery which is equivalent to stages II and III of plastic deformation in alloys of high SFE. In fact, although the SFE is reduced to 24 $mJ.m^{-2}$ by Zn addition, a recovery by climb or cross-slip of dislocations remains possible. After ECAP, a substantial increase in the flow stress is obtained with a remarkable change in the shape of the compression curves. An abrupt decrease of θ is remarked followed by a plateau. On the θ curves, the stage B of twinning which corresponds to the formation of deformation twins is habitually shown by a plateau at $\theta \approx 3$ [41]. The observed plateau is due rather to a competition between strain hardening and recovery by de-twinning on one hand, and to the contribution of the shear bands and the effect of texture on the other hand. In many cases, the plateau is preceded by a slight softening depicted by negative values of θ. The subsequent hardening observed on the θ curves is due to the interaction between moving dislocations and micro- and nano-twin lamellae [67]. This feature is frequently observed in the plateau of twinning in low SFE alloys. The fact that it is presently observed in slipping reveals that the strengthening is due to the twins introduced by ECAP. Furthermore, the effect is more remarked for N=2 where the twin density is maximum (Fig. 4b). Twin hardening can operate through two mechanisms as was proposed: 1) the Hall-Petch mechanism where TB act as GB in reducing the free path of dislocations which is equivalent to a reduction of grain size [53,67-69]. 2) A crystal reorientation: Basinski et al. [70] suggest in Cu-Al alloys, that the increase in strength is the result of transforming dislocations from glissile to sessile configuration in case of the new orientation within twin is unfavorable to slip under external load. Moreover, the TBs introduced by ECAP constitute additional sites for dislocation emission mainly in nc materials where grains are almost free from dislocations. The dislocations nucleate in a TB, cross the twin during deformation and pile up at the next TB; this leads to a fragmentation of twin/matrix lamella and

enhances de-twinning [71] which can explain the subsequent softening observed on the θ curves.

It has been reported that the required stress for generating twins in nc metals can be estimated by [51,71]: $\tau_{twin} = \gamma/\sqrt{3}b + \sqrt{3}Gb/D_G$ where γ is the SFE and D_G the grain size; this means that it is lowered by decreasing γ and increasing D_G. From this equation, no dependence of τ_{twin} on the strain rate and on temperature is expected since all the parameters do not involve thermal activation. The strain rate effect on the twinning stress was rarely studied [72-74]. Moreover, it is believed that increasing SR increases the contribution of twinning to deformation. However, SR effect is generally too low to be considered as an important way for generating twinning even in NC materials since the stress increases by 5 – 10 MPa per order of magnitude of $\dot{\varepsilon}$. In contrast τ_{twin} can be reached by several ways of strengthening like solid solution (SS) or strain hardening. The twin nucleates in steps: the leading partial glides and creates a stacking fault (SF) whereas the trailing twinning partial glides on the adjacent plane. It has been considered that, in the twinning/de-twinning procedure, the dislocation that needs the lowest stress to glide is considered to be active [75]. The GS effect can be summarized as below: As the grain size is reduced, as the number of orientations increases and so does the number of grains reaching the critical stress for the emission of twinning partials. Thus, τ_{twin} was found to be 350 MPa and 254 MPa for CuZn10 (D_G: 75 nm) and CuZn20 (D_G: 59 nm), respectively [61].

4.3. SRS and activation volume

When slipping is the dominant mechanism of deformation, the activation volume is given by: $V^* = d_{fp}.\lambda.b$ [76,77]. d_{fp} is the free path for dislocation movement, λ is the barrier width and b is the magnitude of the Burgers vector. The parameter $\lambda \approx b$ and so, $V^* = d_{fp}.b^2$. The expected strengthening factors in the present alloy are the forest dislocations, sub-boundaries and twin boundaries. d_{fp} can then be expressed by [78]:

$1/d_{fp} = 1/d_{tw} + 1/D + 1/d_d$ (6)

d_{tw} is the twin distance; it is related to the twin density β which is the probability of finding a twin fault between any two neighboring (111) layers: $d_{tw} = d_{111}/\beta$, D the crystallite size i.e. the sub-boundary spacing and d_d the dislocation spacing, $d_d = \rho^{-1/2}$. The values of ρ, β and D are accessible from XRD experiments (Fig. 4). *Table 1* gives the parameters introduced in equation (6) and the calculated values of V* scaled in b^3 and taking b = 0.256nm.

The values obtained for the crystallite size from XRD are of the same order as the grain size obtained from EBSD imaging. The straining effects, i.e the increase of β, ε_{rms}, ρ and the decrease of D are remarked up to N = 2. For N=3 a tendency to recovery is observed. This indicates that many reactions between twins have occurred leading to a de-twinning.

Fig. 9 shows the log-log representation of the dependence of the 0.2% flow stress against the strain rate. The values of the SRS parameter m which represent the slopes of the straight lines, are 0.023, 0.025 and 0.019 for N=1, N=2 and N=3 respectively. These values are much higher than those expected for dislocation based deformation mechanisms; they are consistent rather with deformation by emission of dislocations from GB and TB i.e. the inverse Cottrell-Stokes (ICS) regime [79-81]. In the present alloy, the high twin density observed after ECAP (Fig. 3, 7) promotes the emission of dislocations (perfect $\frac{1}{2} < 110 >$ or Shockley partials $\frac{1}{6} < 112 >$) from TB and GB. For N=0 no sensitivity of the 0.2% flow stress on the strain rate was observed (Fig. 5). The apparent activation volume can be calculated using the equation: $V^* = Mk_BT/m_{app}$ where M is the Taylor factor, k_B the Boltzmann constant, T the testing temperature. $m_{app} = \Delta\sigma/\Delta \mathrm{Ln}\dot{\varepsilon}$ is an apparent SRS parameter which represents the slope of the straight line of the representation σ vs $\mathrm{Ln}\dot{\varepsilon}$. It is worth recalling that the calculation of V* from m_{app} is sensitive to the value chosen for M. In the absence of a direct experimental

determination method, the choice of M can be subjective. M is frequently taken $\sqrt{3}$ in nc metals of random grain orientations. However, it has been reported that for the cfc γ-phase in a α/γ duplex steel of fibrous morphology, comparable to that in the present alloy (Fig. 3, 8), M ranges between 3 and 4 [82]. Taking M = 3, k_B =1.38.10^{-23}J.K^{-1}, T = 298°C, we obtain values of V* of 1.8 nm^3 (105 b^3), 1.2 nm^3 (71 b^3)and 1.7 nm^3 (100 b^3) for N = 1, N = 2 and N = 3 respectively. These values are close to those estimated from the XRD results and confirm that micro- and nano-twins contribute to strengthening. On the other hand, we can conclude that the increase of V* for N=3 is due to a de-twinning since the interaction of perfect or partial dislocations with the twins and the SFs restricts the recovery by climb or annihilation.

4.4. Comparison with nanoindentation (NI) results

The rapid decrease of H for the depths below 800 nm (Fig. 6) is due, among others, to a transient microstructure and/or to surface roughness and screens the effect of the SRJ. The depth-independent hardness beyond 800 nm (Fig.6) indicates rather a more stable microstructure so that, according to equation (2), the measured hardness H merges with the bulk hardness Ho. As a result, the SR dependence of H_{NI} is clearer and only this part of the curve was considered in the calculations. The log-log plot of Fig. 10 shows a good linear fitting of Ho against the SR; the SRS parameter was calculated to be m=0.025. This value depicts an important contribution of grain boundary sliding. In Cu-X alloys processed by HPT, Bruder et al. [5] have obtained a depth-independent hardness only from a depth 500nm in Cu Zn and Cu-Sn alloys. The SRS obtained was m=0.028 in Cu-5%Zn whereas it was 0.011 in Cu-3%Sn although the solid solution (SS) effect of Sn was estimated to be 3.4 time stronger than that of Zn [5]. They suggest a coupled dislocation and GB migration in Cu-Zn alloy and GB mediated dislocation mechanisms in Cu-Sn. The classic SS effect seems have no effect

on the saturation grain size d_s and on SRS. Furthermore, it has been shown that the annihilation of dislocations at GBs are the rate-controlling mechanism [83,84].

A comparison between NI and compression results is allowed regarding the relation between the two scales. Thus, Zhu et al. [85] reported that for an ideal correction factor, the ratio of the Vickers hardness HV by the NI one Ho equals HV/Ho = 0.93 (both in MPa) whereas ratios of 0.65 to 0.79 were obtained in Fe-Cr alloys [86-88]. Furthermore, in materials that do not exhibit high strain hardening, HV = $3\sigma_{0.2}$ (both in MPa) and as a result, one obtains a ratio $\sigma_{0.2}$/ Ho of 0.217 to 0.333. Taking the values of the present study for N = 3, $\sigma_{0.2}$ = 396 MPa for $\dot{\varepsilon}$ = 0.003 s^{-1} in compression and the mean value of Ho values for $\dot{\varepsilon}$ = 0.001 s^{-1} and 0.01 s^{-1} ≈ 2476MPa, , we obtain a ratio of≈ 0.16 which is comparable with the value 0.217 cited above regarding the uncertainties arising from the scale changes. The activation volume V^*_{NI} is obtained by using the formula [89]: $V^* = 3k_BT/(0.16\ \frac{\partial H_o}{\partial Ln\dot{\varepsilon}})$ where $\frac{\partial H_o}{\partial Ln\dot{\varepsilon}}$ is the slope of the straight line of the $H_o - Ln\dot{\varepsilon}$ representation (Fig.10). By considering the slope $\frac{\partial H_o}{\partial Ln\dot{\varepsilon}}$ = 63.5 MPa, the value obtained for N=3 is V*=1.2 nm^3 which corresponds to $73b^3$. This value is comparable with those obtained from compression tests and points a similarity of the mechanisms of deformation involved. The higher values of V* as were calculated from the data of table 1 are due to an overestimation of the dislocation free path since other factors can contribute to pinning like solute atoms. Furthermore, it has been shown that this effect is more important at low SR where the waiting time for dislocations the overcome a barrier is sufficient for solute atoms to segregate and pin the dislocations [81].

5. Conclusions

In the present work, EBSD, XRD, compression and nanoindentation (NI) tests were used to characterize the microstructure and the SRS of Cu-6wt%Zn alloy after ECAP.

1) For N=3, EBSD images revealed a tendency to a fibrous microstructure and a high density of twins that nucleates from GBs. A fragmentation of twins (de-twinning) produces grains 100nm in size.
2) XRD results showed that the maximum twin density was reached for N=2 then a de-twinning takes place.
3) Imaging with a step size of 100 nm revealed grains 100-200nm in size within shear bands even though the extent of refinement was not clearly resolved for the step size used. De-twinning may be the involved mechanism.
4) Compression tests showed that since N=1, deformation occurs by slipping with a hardening effect of ECAP-induced twins. The shape of the curves is consistent with a shear banding.
5) SRS experiments in compression and NI lead to an activation volume of 70b3 - 100b3 consistent with the regime of emission of dislocations from GBs and TBs and agrees with the values estimated from XRD results.

References

[1] P.V. Liddicoat, X.Z. Liao, Y.H. Zhao, Y.T. Zhu, M.Y. Murashkin, E.J. Lavernia, R.Z. Valiev, S.P. Ringer, Nanostructural hierarchy increases the strength of aluminium alloys Nat. Commun. 1 (2010). https://doi.org/10.1038/ncomms1062

[2] K. Lu, L. Lu and S. Suresh, Strengthening Materials by Engineering Coherent Internal Boundaries at the Nanoscale, Science 324 (2009) 349-352. https://doi.org/10.1126/science.1159610

[3] G. Sakai, Z. Horita, T.G. Langdon, Grain refinement and superplasticity in an aluminum alloy processed by high-pressure torsion, Mater. Sci. Eng A 393 (2005) 344–351. https://doi.org/10.1016/j.msea.2004.11.007

[4] C.J. Shute, B.D. Myers, S. Xie, T.W. Barbee Jr., A.M. Hodge, J.R. Weertman, Microstructural stability during cyclic loading of multilayer copper/copper samples with nanoscale twinning, Scr. Mater. 60 (2009) 1073–1077. https://doi.org/10.1016/j.scriptamat.2008.11.049

[5] E. Bruder, P. Braun, H. ur Rehman, R.K.W. Marceau, A. Taylor, R. Pippan, K. Durst, Influence of solute effects on the saturation grain size and rate sensitivity in Cu-X alloys, Scr. Mater. 144 (2018) 5–8, https://doi.org/10.1016/j.scriptamat.2017.09.031

[6] L. Balogh, T. Ungár, Y. Zhao, Y.T. Zhu, Z. Horita, C. Xu, T.G. Langdon, Influence of stacking-fault energy on microstructural characteristics of ultrafine-grain copper and copper–zinc alloys, Acta Mater. 56 (2008) 809. https://doi.org/10.1016/j.actamat.2007.10.053

[7]] M. Hafok, R. Pippan, Influence of stacking fault energy and alloying on stage V hardening of HPT-deformed materials, Int. J. Mater. Res. 101 (2010) 1097. http://dx.doi.org/10.3139/146.110389

[8] X.H. An, Q.Y. Lin, S.D. Wu, Z.F. Zhang, R.B. Figueiredo, N. Gao, T.G. Langdon, The influence of stacking fault energy on the mechanical properties of nanostructured Cu and Cu–Al alloys processed by high-pressure torsion. Scr. Mater. 64 (2011) 954, https://doi.org/10.1016/j.scriptamat.2011.01.041

[9] C.X. Huang, W. Hu, G. Yang, Z.F. Zhang, S.D. Wu, Q.Y. Wang, G. Gottstein, The effect of stacking fault energy on equilibrium grain size and tensile properties of nanostructured copper and copper–aluminum alloys processed by equal channel angular pressing, Mater. Sci. Eng A 556 (2012) 638–647. http://dx.doi.org/10.1016/j.msea.2012.07.041

[10] F.A. Mohamed, A dislocation model for the minimum grain size obtainable by milling, Acta Mater. 51 (2003) 4107. https://doi.org/10.1016/S1359-6454(03)00230-1

[11] S. Qu, X.H. An, H.J. Yang, C.X. Huang, G. Yang, Q.S. Zang, Z.G. Wang, S.D. Wu, Z.F. Zhang, Microstructural evolution and mechanical properties of Cu–Al alloys subjected to equal channel angular pressing, Acta Mater. 57 (2009) 1586. https://doi.org/10.1016/j.actamat.2008.12.002

[12] H. Bahmanpour, K.M. Youssef, J. Horky, D. Setman, M.A. Atwater, M.J. Zehetbauer, R.O. Scattergood, C.C. Koch, Deformation twins and related softening behavior in nanocrystalline Cu–30% Zn alloy, Acta Mater. 60 (2012) 3340. https://doi.org/10.1016/j.actamat.2012.02.036

[13] Z.J. Zhang, Q.Q. Duan, X.H. An, S.D. Wu, G. Yang, Z.F. Zhang, Microstructure and mechanical properties of Cu and Cu–Zn alloys produced by equal channel angular pressing,Mater. Sci. Eng. A 528 (2005) 4259. https://doi.org/10.1016/j.msea.2010.12.080

[14] F. Wu, H.M. Wen , E.J. Lavernia , J. Narayan, Y.T. Zhu, Twin intersection mechanisms in nanocrystalline fcc metals, Mater. Sci. Eng. A 585 (2013) 292–296 https://doi.org/10.1016/j.msea.2013.07.063

[15] P. Zhou, Z.Y. Liang, R.D. Liu, M.X. Huang, Evolution of dislocations and twins in a strong and ductile nanotwinned steel Acta Materialia 111 (2016) 96-107. https://doi.org/10.1016/j.actamat.2016.03.057

[16] A.A.S. Mohammed, E.A. El-Danaf, A.A. Radwan, Equivalent twinning criteria for FCC alloys under uniaxial tension at high temperatures Mater. Sci. Eng. A 457 (2007) 373–379. https://doi.org/10.1016/j.msea.2006.12.113

[17] Y.T. Zhu, X.Z. Liao, X.L. Wu, Deformation twinning in nanocrystalline materials Prog. Mater. Sci. 57 (2012) 1–62. http://dx.doi.org/10.1016/j.pmatsci.2011.05.001

[18] V. Yamakov, D. Wolf, S.R. Phillpot, A.K. Mukherjee, H. Gleiter, Dislocation processes in the deformation of nanocrystalline aluminium by molecular-dynamics simulation, Nat. Mater. 1 (2002) 45–49. https://doi.org/10.1038/nmat700

[19] M.A. Meyers MA, O.Vohringer, V.A. Lubarda, The onset of twinning in metals: A constitutive description. Acta Mater. 49 (2001) 4025–39, https://doi.org/10.1016/S1359-6454(01)00300-7

[20] L. Balogh, T. Ungar, Y.H. Zhao, Y.T. Zhu, Z. Horita, C. Xu, T.G. Langdon, Influence of stacking-fault energy on microstructural characteristics of ultrafine-grain copper and copper–zinc alloys, Acta Mater. 56 (2008) 809. https://doi.org/10.1016/j.actamat.2007.10.053

[21] Y.H. Zhao, X.Z. Liao, Y.T. Zhu, Z. Horita, T.G. Langdon, Influence of stacking fault energy on nanostructure formation under high pressure torsion, Mater. Sci. Eng. A 410–411 (2005) 188. https://doi.org/10.1016/j.msea.2005.08.074

[22] X.Z. Liao, Y.H. Zhao, S.G. Srinivasan, Y.T. Zhu, R.Z. Valiev, D.V. Gunderov, Deformation twinning in nanocrystalline copper at room temperature and low strain rate, Appl Phys Lett 84 (2004) 592. https://doi.org/10.1063/1.1644051

[23] X.L. Wu, Y.T. Zhu, E. Ma 2006. Predictions for partial-dislocation-mediated processes in nanocrystalline Ni by generalized planar fault energy curves: an experimental evaluation. Appl. Phys. Lett. 88 (2006) 121905. http://dx.doi.org/10.1063/1.2186968

[24] I.J. Beyerlein, X. Zhang, A. Misra, Growth Twins and Deformation Twins in Metals, Annu. Rev. Mater. Res. 44 (2014) 329–63, https://doi.org/10.1146/annurev-matsci-070813-113304

[25] S. Mahajan, Critique of mechanisms of formation of deformation, annealing and growth twins: Face-centered cubic metals and alloys, Scr. Mater. 68 (2013) 95–99. https://doi.org/10.1016/j.scriptamat.2012.09.011

[26] Z.W. Wang, Y.B. Wang, X.Z. Liao, Y.H. Zhao, E.J. Lavernia, Y.T. Zhu, Z. Horita, T.G. Langdon, Influence of stacking fault energy on deformation mechanism and dislocation storage capacity in ultrafine-grained materials, Scr. Mater. 60 (2009) 52–55. https://doi.org/10.1016/j.scriptamat.2008.08.032

[27] J. Wang, N. Li, O. Anderoglu, X. Zhang, A. Misra, J.Y. Huang, J.P. Hirth, Detwinning mechanisms for growth twins in face-centered cubic metals, Acta Mater. 58 (2010) 2262–2270. https://doi.org/10.1016/j.actamat.2009.12.013

[28] C.S. Hong, N.R. Tao, X. Huang, K. Lu, Nucleation and thickening of shear bands in nano-scale twin/matrix lamellae of a Cu–Al alloy processed by dynamic plastic deformation, Acta Mater. 58 (2010) 3103–3116. https://doi.org/10.1016/j.actamat.2010.01.049

[29] S. Ni, Y.B. Wang, X.Z. Liao, R.B. Figueiredo, H.Q. Li, S.P. Ringer, T.G. Langdon, Y.T. Zhu, The effect of dislocation density on the interactions between dislocations and twin boundaries in nanocrystalline materials, Acta Mater. 60 (2012) 3181–3189. https://doi.org/10.1016/j.actamat.2012.02.026

[30] A.M. Hodge, T.A. Furnish, C.J. Shute, Y. Liao, X. Huang, C.S. Hong, Y.T. Zhu, T.W. Barbee Jr., J.R. Weertman, Twin stability in highly nanotwinned Cu under compression, torsion and tension, Scr. Mater. 66 (2012) 872–877. https://doi.org/10.1016/j.scriptamat.2012.01.027

[31] C.J. Shute, B.D. Myers, S. Xie, S.Y. Li, T.W. Barbee Jr, A.M. Hodge, J.R. Weertman, Detwinning, damage and crack initiation during cyclic loading of Cu samples containing aligned nanotwins, Acta Mater. 59 (2011) 4569–4577. https://doi.org/10.1016/j.actamat.2011.04.002

[32] Y. Wei, The kinetics and energetics of dislocation mediated de-twinning in nano-twinned face-centered cubic metals, Mater. Sci. Eng.: A 528 (2011) 1558–1566. https://doi.org/10.1016/j.msea.2010.10.072

[33] O. Anderoglu, A. Misra, J. Wang, R.G. Hoagland, J.P. Hirth, X. Zhang, Plastic flow stability of nanotwinned Cu foils, Int. J. Plasticity 26 (2010) 875–886. https://doi.org/10.1016/j.ijplas.2009.11.003

[34] J. Hu, J. Zhang, Z. Jiang, X. Ding, Y. Zhang, S. Han, J. Sun, J. Lian, Plastic deformation behavior during unloading in compressive cyclic test of nanocrystalline copper, Mater. Sci. Eng. A 651 (2016) 999-1009. https://doi.org/10.1016/j.msea.2015.11.031

[35] Y. Jiang, J. Hu, Z. Jiang, J. Lian, C. Wen, Strain rate dependence of tensile strength and ductility of nano and ultrafine grained coppers, Mater. Sci. Eng. A 712 (2018) 341-349. https://doi.org/10.1016/j.msea.2017.11.083

[36] P. Spätig, J. Bonneville, J.-L. Martin, A new method for activation volume measurements: application to Ni_3(Al, Hf), Mater. Sci. Eng. A 167 (1993) 73-79. https://doi.org/10.1016/0921-5093(93)90339-G

[37] X. Chen, C. Liu, Y. Wan, S. Jiang, Z. Chen, Y. Zhao, Grain refinement mechanisms in gradient nanostructured AZ31B Mg alloy prepared via rotary swaging, Metall. Mater. Trans. A 52 (2021) 4053–4065, https://doi.org/10.1007/s11661-021-06364-9

[38] H. Huang, H. Liu, L.S. Wang, Y.H. Li, S.O. Agbedor, J. Bai, F. Xue, J.H. Jiang, A high strength and biodegradable Zn-Mg alloy with refined tenary eutectic structure processed by ECAP, Acta Metall. Sin. Engl. Lett. (2020), http://doi.org/10.1007/s40195-020-01027-x

[39] H. Huang, H. Liu, L. Wang, K. Yan, Y. Li , J. Jiang, A. Ma, F. Xue, J. Bai, Revealing the effect of minor Ca and Sr additions on microstructure evolution and mechanical properties of Zn-0.6 Mg alloy during multi-pass equal channel angular pressing, J. Alloys Compd. 844 (20120) 155923, https://doi.org/10.1016/j.jallcom.2020.155923

[40] S.N. Dey, P. Chatterjee, S.P Sen Gupta, Study of deformation stacking faults and dislocation microstructures in Cu–1Sn–Zn alloys, Acta Mater. 53 (2005) 4635-4642. https://doi.org/10.1016/j.actamat.2005.06.017

[41] E. El-Danaf, S. R. Kalidindi, R.D. Doherty, Influence of Grain Size and Stacking-Fault Energy on Deformation Twinning in Fcc Metals. Metal. Mater. Trans. A 30 (1999) 1223-1233. https://doi.org/10.1007/s11661-999-0272-9

[42] V.M. Segal, Equal channel angular extrusion: from macromechanics to structure formation, Mater. Sci. Eng. A 271 (1999) 322–333, https://doi.org/10.1016/S0921-5093(99)00248-8

[43] Y. Iwahashi, J. Wang, Z. Horita, M. Nemoto, T.G. Langdon, Principle of equal channel angular pressing for the processing of ultra-fine grained materials, Scr. Mater. 35 (1996) 143–146, https://doi.org/10.1016/1359-6462(96)00107-8

[44] Y. Iwahashi, Z. Horita, M. Nemoto, T.G. Langdon, The process of grain refinement in equal-channel angular pressing, Acta Mater. 46 (1998) 3317–3331, https://doi.org/10.1016/S1359-6454(97)00494-1

[45] Y.W. Chen, Y.T. Tsai, P.Y. Tung, S.P. Tsai, C.Y. Chen, S.H. Wang, J.R. Yang, Phase quantification in low carbon Nb-Mo bearing steel by electron backscatter diffraction technique coupled with kernel average misorientation, Mater. Charact. 139 (2018) 49–58, https://doi.org/10.1016/j.matchar.2018.01.041

[46] P.J. Konijnenberg, S. Zaefferer, D. Raabe, Assessment of geometrically necessary dislocation levels derived by 3D EBSD, Acta Mater. 99 (2015) 402–414, https://doi.org/10.1016/j.actamat.2015.06.051

[47] J. Alkorta, J. M. Martínez-Esnaola, J. G. Sevillano, Critical examination of strain-rate sensitivity measurement by nanoindentation methods: Application to severely deformed niobium, acta mater 56 (2008) 884-893. https://doi.org/10.1016/j.actamat.2007.10.039

[48] V. Maier, K. Durst, J. Mueller, B. Backes, H. W. Höppel, M. Göken, Nanoindentation strain-rate jump tests for determining the local strain-rate sensitivity in nanocrystalline Ni and ultrafine-grained Al, J. Mater. Res. 26 (2011) 1421-1430. https://doi.org/10.1557/jmr.2011.156

[49] W.D. Nix, H. Gao, Indentation size effects in crystalline materials: a law for strain gradient plasticity, J. Mech. Phys. Solids. 46 (3) (1998) 411–425. https://doi.org/10.1016/S0022-5096(97)00086-0

[50] M. Niewczas and G. Saada, Twinning nucleation in Cu-8 at.% Al single crystals. Philos Mag A. 82 (2002) 161. https://doi.org/10.1080/01418610208240003

[51] T. Ungar, J. Gubicza, Nanocrystalline materials studied by powder diffraction line profile analysis, Z. Kristallogr. 222 (2007) 114-128. https://doi.org/10.1524/zkri.2007.222.3-4.114

[52] V. Biju, N. Sugathan, V. Vrinda, S. L. Salin, Estimation of lattice strain in nanocrystalline silver from X-ray diffraction line broadening J. Mater Sci (2008) 43:1175–1179. http://dx.doi.org/10.1007/s10853-007-2300-8

[53] S. Mahajan and G.Y. Chin, Formation of deformation twins in f.c.c. crystalsFormation des macles de deformation dans les cristaux c.f.c. Acta Metallurgica Volume 21 1973, Pages 1353-1363. https://doi.org/101016/0001-6160(73)90085-0

[54] Y.H. Zaho, Y.T. Zhu, X.Z. Liao, Z. Horita, T.G. Longdon, Tailoring stacking fault energy for high ductility and high strength in ultrafine grained Cu and its alloy, Appl. Phys. Lett. 89 (2006) 121906. https://doi.org/10.1063/1.2356310

[55] Y.H. Zaho, Z. Horita, T.G. Longdon, Y.T. Zhu, Evolution of defect structures during cold rolling of ultrafine-grained Cu and Cu–Zn alloys: Influence of stacking fault energy, Mater. Sci. Eng. A 474(1-2) (2008) 342-347. https://doi.org/10.1016/j.msea.2007.06.014

[56] L. Velterop, R. Delhez, Th. H. de Keijser, E. J. Mittemeijer, D. Reefman, X-ray diffraction analysis of stacking and twin faults in f.c.c. metals: a revision and allowance for texture and non-uniform fault probabilities. J. Appl. Cryst. 33 (2000) 296-306. https://doi.org/10.1107/S0021889800000133

[57] X.K. Zhang, X.Y. Yang, W. Chen, J. Qin, J.P. Fouse, Effect of stacking fault energy on mechanical properties and annealing behavior of brasses, J. Alloy Compd. 679 (2016) 400-407. https://doi.org/10.1016/j.jallcom.2016.04.083

[58] X.X. Wu, X.Y. San, X.G. Liang, Y.L. Gong, X.K. Zhu, Effect of stacking fault energy on mechanical behavior of cold-forging Cu and Cu alloys, Mater. Des. 47 (2013) 372–376. http://doi.org/10.1016/j.matdes.2012.12.006

[59] S.M. Dasharath, S. Mula, Microstructural evolution and mechanical properties of low SFE Cu-Al alloys processed by cryorolling followed by short-annealing, Mater. Des. 99 (2016) 552–564, http://doi.org/10.1016/j.matdes.2016.03.095

[60] Z. Zribi, H.H. Ktari, F. Herbst, V. Optasanu, N. Njah, EBSD, XRD and SRS characterization of a casting Al-7wt%Si alloy processed by equal channel angular extrusion: Dislocation density evaluation, Mater. Charact. 153 (2019) 190–198, https://doi.org/10.1016/j.matchar.2019.04.044

[61] Y.T. Zhu, X.Z. Liao, X.L. Wu, Deformation twinning in bulk Nanocrystalline metals: Experimental observations, JOM 60 (2008) 60-64. https://doi.org/10.1007/s11837-008-0120-1

[62] K. Lu, J. Lu, Surface Nanocrystallization (SNC) of Metallic Materials-Presentation of the Concept behind a New Approach, J Mater Sci Technol 15 (1999) 197. https://www.jmst.org/EN/Y1999/V15/I03/193

[63] Y.T. Zhu, X.L. Wu, X.Z. Liao, J. Narayan, S.N. Mathaudhu, L.J. Kecskes, Twinning partial multiplication at grain boundary in nanocrystalline fcc metals, Appl Phys Lett. 95 (2009) 031909. https://doi.org/10.1063/1.3187539

[64] E. El-Danaf, S.R. Kalidindi, R.D. Doherty, C. Necker, Deformation texture transition in brass: critical role of micro-scale shear bands, Acta Mater. 48 (2000) 2665. https://doi.org/10.1016/S1359-6454(00)00050-1

[65] Z. Jasien´ski, H. Paul, A. Pia¸tkowski, A. Litwora, Microstructure and Texture of Copper Single Crystal of (112)[1 1 1] Orientation Undergoing Channel-Die Compression at 77 K. J. Mater. Proc. Technol. 53 (1995) 187. http://dx.doi.org/10.1016/0924-0136(95)01975-K

[66] H. Paul, J.H. Driver, C. Maurice, Z. Jasieński , Shear band microtexture formation in twinned face centred cubic single crystals, Mater. Sci. Eng. A 359 (2003) 178-191. https://doi.org/10.1016/S0921-5093(03)00335-6

[67] A.A. Salem, S.R. Kalidindi, R.D. Doherty, S.L. Semiatin, Strain Hardening Due to Deformation Twinning in α-Titanium: Mechanisms, Metal. Mater. Tans. A 37 (2006) 259-268. https://doi.org/10.1007/s11661-006-0171-2

[68] E.O. Hall, The Deformation and Ageing of Mild Steel: III Discussion and Results. Proc. Phys. Soc. B 64 (1951) 747-753. https://doi.org/10.1088/0370-1301/64/9/303

[69] N. J. Petch, The Cleavage Strength of Polycrystals, J. Iron Steel Inst., 1953, vol. 174, pp. 25-28.

[70] Z.S. Basinski, M.S. Szczerba, M. Niewczas, J.D. Embury, and S.J. Basinski, The transformation of slip dislocations during twinning of copper-aluminum alloy crystals, Rev. Metall. 94 (1997) 1037-43. http://dx.doi.org/10.1051/metal/199794091037

[71] B. Roy, T. Maity, J. Das, Tuning of nanostructure by the control of twin density, dislocation density, crystallite size, and stacking fault energy in $Cu_{100-x}Zn_x$ (0<x<30 wt%), Mater. Sci. Eng. A 672 (2016) 203–215. https://doi.org/10.1016/j.msea.2016.07.016

[72] A. Rohatgi, K. S. Vecchio, T. Gray, The influence of stacking fault energy on the mechanical behavior of Cu and Cu-Al alloys: Deformation twinning, work hardening, and dynamic recovery, Metal. Mater. Trans. A 32 (2001) 135–145 http://dx.doi.org/10.1007/s11661-001-0109-7

[73] M.A. Crimp, B.C. Smith, and D.E. Mikkola, Substructure development in shock-loaded Cu-8.7 Ge and copper: the role of temperature, grain size and stacking fault energy. Mater. Sci. Eng. A 96 (1987) 27-40. https://doi.org/10.1016/0025-5416(87)90537-4

[74] G.T. Gray III, P.S. Follansbee, and C.E. Frantz, Effect of residual strain on the substructure development and mechanical response of shock-loaded copper. Mater. Sci. Eng.A 111 (1989) 9-16. https://doi.org/10.1016/0921-5093(89)90192-5

[75] Y. T. Zhu, X. Z. Liao, X. L. Wu, J. Narayan, Grain size effect on deformation twinning and detwinning, J Mater. Sci. 48 (2013) 4467–4475. http://dx.doi.org/10.1007/s10853-013-7140-0

[76] Q. Wei, S. Cheng, K.T. Ramesh, E. Ma, Effect of nanocrystalline and ultrafine grain sizes on the strain rate sensitivity and activation volume: fcc versus bcc metals, Mater. Sci. Eng. A 381 (2004) 71–79, https://doi.org/10.1016/j.msea.2004.03.064

[77] S.L. Yan, H. Yang, H.W. Li, X. Yao, Variation of strain rate sensitivity of an aluminum alloy in a wide strain rate range: mechanism analysis and modeling, J. Alloys Compd. 688 (2016) 776–786, https://doi.org/10.1016/j.jallcom.2016.07

[78] Z. Trojanová, Z. Drozd, P. Luká ˇc, J. Džugan, Studying the Thermally Activated Processes Operating during Deformation of hcp and bcc Mg–Li Metal-Matrix Composites, , Metals 11 (2021) 473, https://doi.org/10.3390/met11030473

[79] C. Duhamel, Y. Bréchet, Y. Champion, Activation volume and deviation from Cottrell–Stokes law at small grain size, Int. J. Plast. 26 (2010) 747–757, https://doi.org/10.1016/j.ijplas.2009.10.003

[80] Y. Champion, Competing regimes of rate dependent plastic flow in ultrafine grained metals, Mater. Sci. Eng. A 560 (2013) 315–320, https://doi.org/10.1016/j.msea.2012.09.072

[81] A. Soula, J.P. Couzinié, H. Heni, J. Bourgon, Y. Champion, N. Njah, Activation volume and the role of solute atoms in Al-Mg-Si alloy processed by equal channel angular extrusion, J. Alloy Compd. 899 (2022) 163334. https://doi.org/10.1016/j.jallcom.2021.163334

[82] A. Sarkar, S. Sanyal, T.K. Bandyopadhyay, S. Mandal, Implications of microstructure, Taylor factor distribution and texture on tensile properties in a Ti-added Fe-Mn-Al-Si-C steel, Mater. Sci. Eng. A 767 (2019) 138402, https://doi.org/10.1016/j.msea.2019.138402

[83] W. Blum, X. H. Zeng, A simple dislocation model of deformation resistance of ultrafine-grained materials explaining Hall–Petch strengthening and enhanced strain rate sensitivity, acta Mater. 57 (2009) 1966. https://doi.org/10.1016/j.actamat.2008.12.041

[84] Z. Sun, S. Van Petegem, A. Cervellino, K. Durst, W. Blum, H. Van Swygenhoven, Dynamic recovery in nanocrystalline Ni**,** acta Mater. 91 (2015) 91-100. https://doi.org/10.1016/j.actamat.2015.03.033

[85] P. Zhu, Y. Zhao, S. Agarwal, J. Henry, S.J. Zinkle, Toward accurate evaluation of bulk hardness from nanoindentation testing at low indent depths, Mater Des 213 (2022) 110317. https://doi.org/10.1016/j.matdes.2021.110317

[86] Y. Yang, C. Zhang, Z. Ding, C. Su, T. Yan, Y. Song, Y. Cheng, A correlation between micro- and nano-indentation on materials irradiated by high-energy heavy ions, J. Nucl. Mater. 498 (2018) 129–136. https://doi.org/10.1016/j.jnucmat.2017.10.025

[87] K. Yabuchi, Y. Kuribayashi, S. Nogami, R. Kasada, A. Hasegawa, Evaluation of irradiation hardening of proton irradiated stainless steels by nanoindentation, J. Nucl. Mater. 446 (2014) 142–147. https://doi.org/10.1016/j.jnucmat.2013.12.009

[88] S. Chen, Y. Miyahara, A. Nomoto, K. Nishida, Effects of thermal aging and low fluence neutron irradiation on the mechanical property and microstructure of ferrite in cast austenitic stainless steels, Acta. Mater. 179 (2019) 61–69. https://doi.org/10.1016/j.actamat.2019.08.029

[89] A.A. Elmustafa, D.S. Stone, Size-dependent hardness in annealed and work hardened α-brass and aluminum polycrystalline materials using activation volume analysis, Mater. Lett. 57 (2003) 1072-1078. https://doi.org/10.1016/S0167-577X(02)00933-3

Figure captions

Fig. 1: ECAP sample (Dashed cylinder) and specimens for compression tests. EBSD and XRD were carried out on X plane as is defined.

Fig. 2: IPF of the alloy as quenched with the color key for the cubic crystal orientation maps (a) and after ECAP for 3 passes (b) recorded on the X plane. Blue zones correspond to deformation twins

Fig. 3: Microstructure of the alloy as revealed by the UGC (a), IQ (b) and the KAM cartography (c). Color code for KAM converted to dislocation density (see text) is given in d. Selected zone is magnified in Fig. 7 (discussion section).

Fig. 4: (a): Diffraction spectra of the alloy for N=0 and N=3 with a magnification of the (111) and (200) peaks. (b) Crystallite size D, rms strain ε_{rms} , dislocation density ρ and twin density β calculated from XRD as a function of N.

Fig. 5: True stress – true strain σ (ε) and the normalized hardening rate θ (ε) curves in compression for different numbers of passes recorded at different strain rates.

Fig. 6: Selected nanoindentation force-depth F(h) curves of the alloy for N=3 at different strain rates. Creep behavior is depicted by the plateau at SR 25.10^{-4} to 25.10^{-2} s^{-1}(see the inserts).

Fig. 7: A magnification of the selected zone of Fig. 3 (IQ and UGC) showing twins of different colors from the parent grain and starting from GB (white arrows), fine grains in α fibers (black arrows) and in twin lamella (white arrows).

Fig. 8: IQ, IPF and UGC at high magnification (step size 0.1µm): Dark zones of low IQ correspond to α fibers characterized by fine grains. Several deformation twins are arrowed on the IPF (b).

Fig. 9: The Ln-Ln representation of the 0.2% flow stress $\sigma_{0.2}$ in compression (in MPa) for N=1 to N=3.

Fig. 10: Linear and logarithmic plots of the nanoindentation bulk hardness Ho (in MPa) for N=3 as a function of the strain rate.

Fig.1:

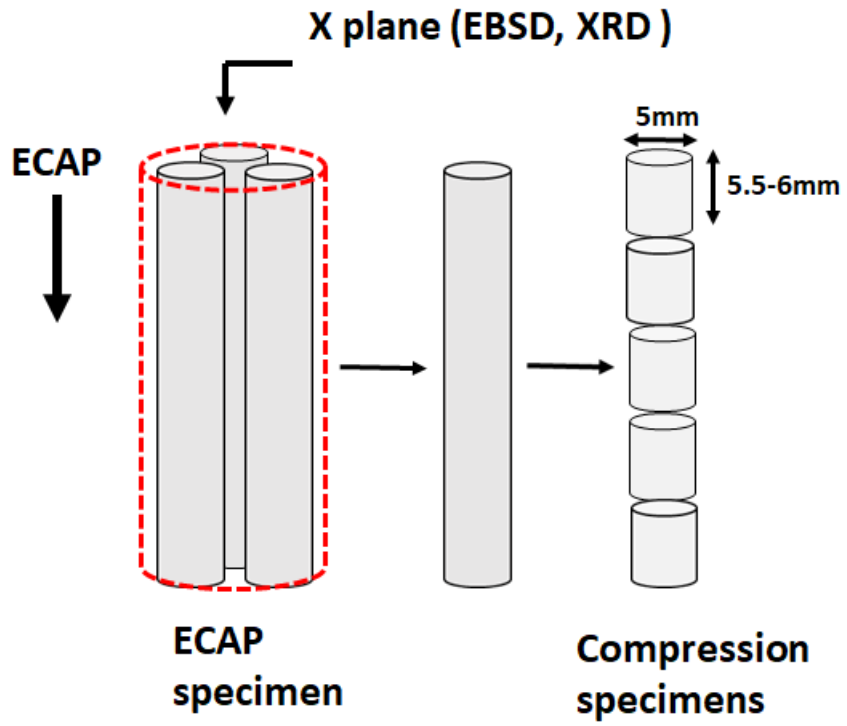
X plane (EBSD, XRD)
ECAP
5mm
5.5-6mm
ECAP specimen
Compression specimens

Fig.2:

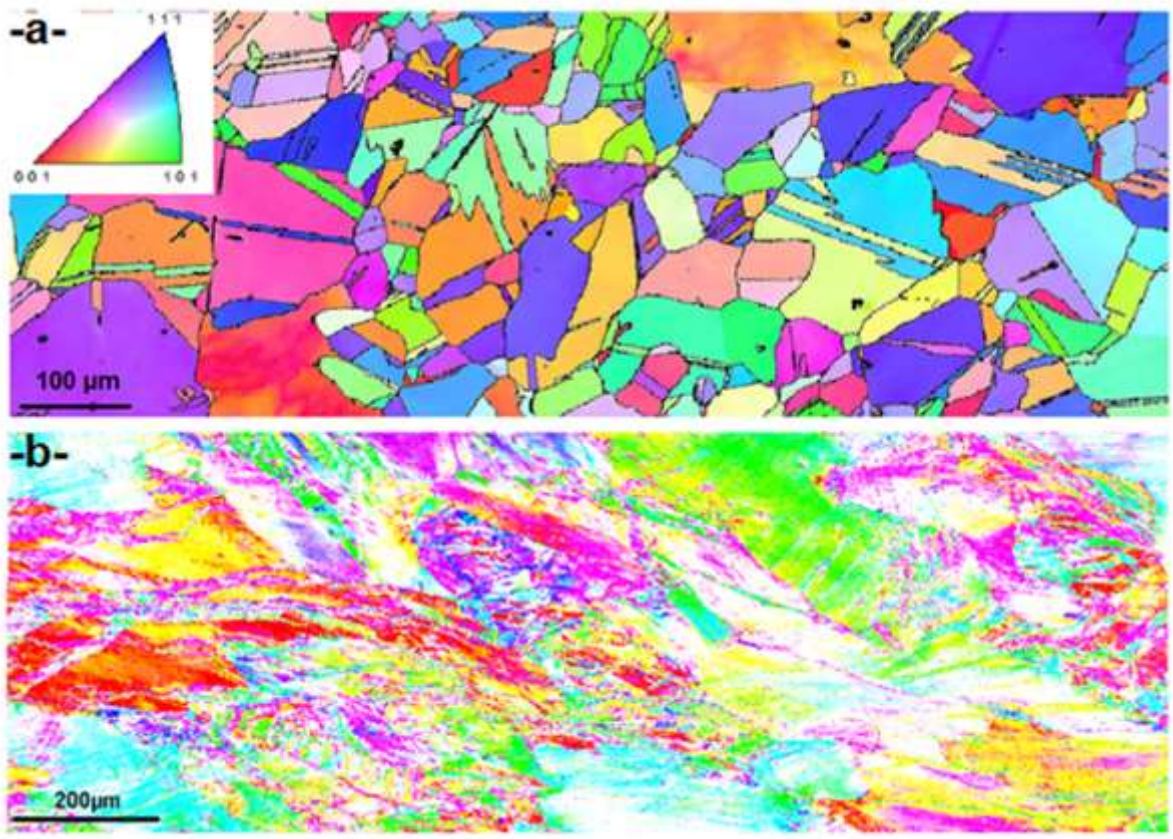

Fig.3:

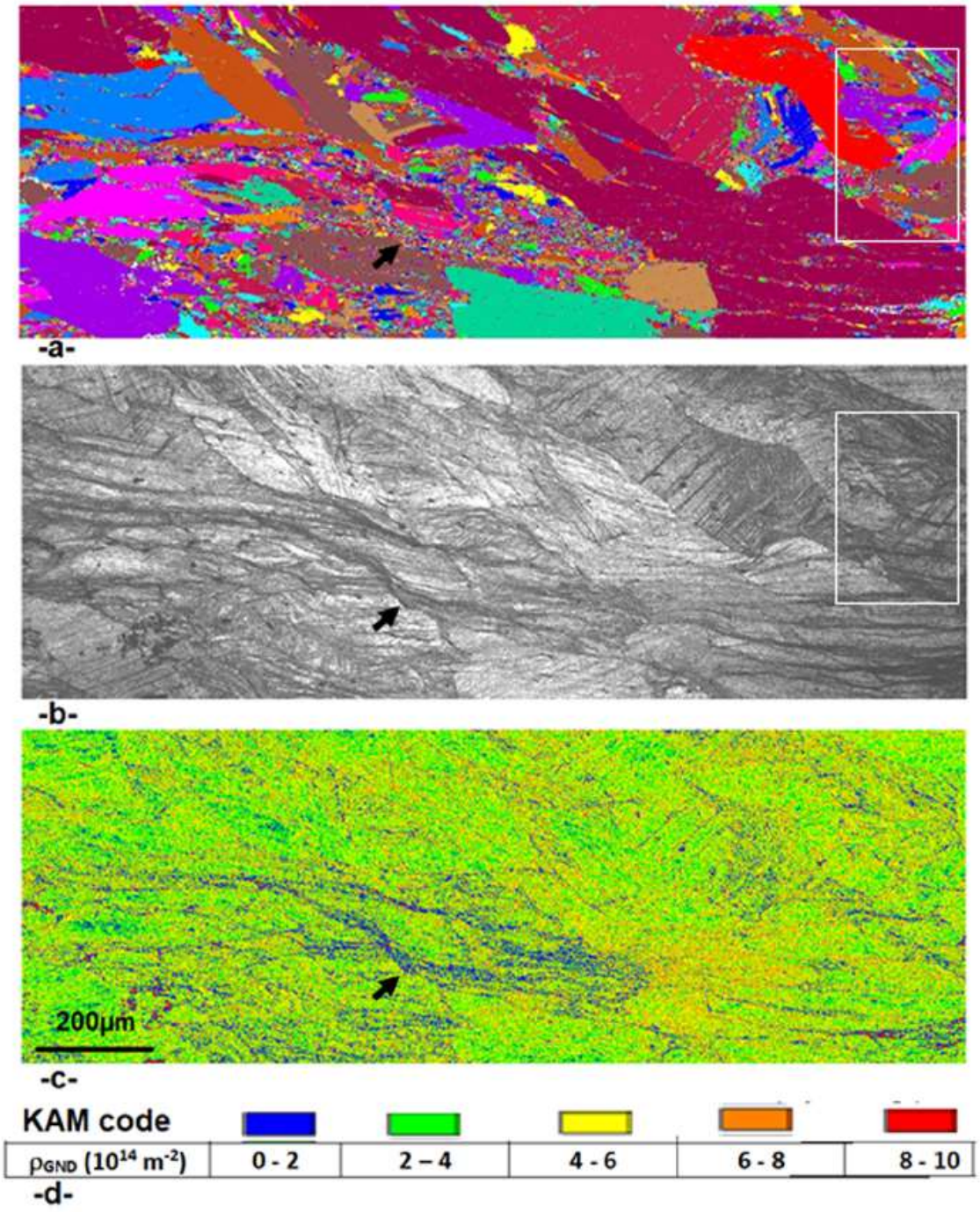

Fig.4:

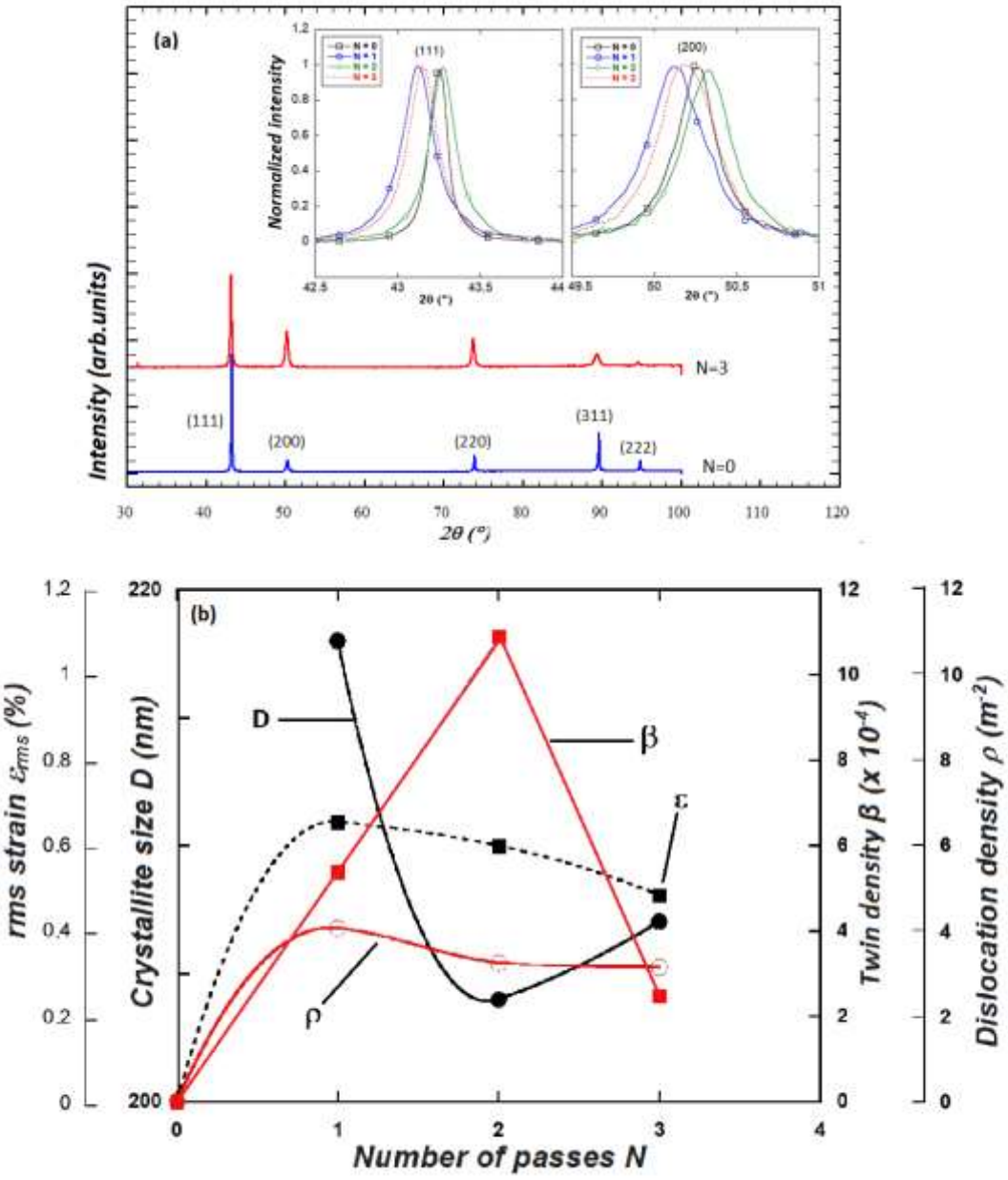
(a)
Normalized intensity
(111)
(200)
2θ (°)
Intensity (arb.units)
N=3
N=0
(111)
(200)
(220)
(311)
(222)
2θ (°)
(b)
D
β
ε
ρ
rms strain ε_{rms} (%)
Crystallite size D (nm)
Twin density β (x 10^{-4})
Dislocation density ρ (m^{-2})
Number of passes N

Fig.5:

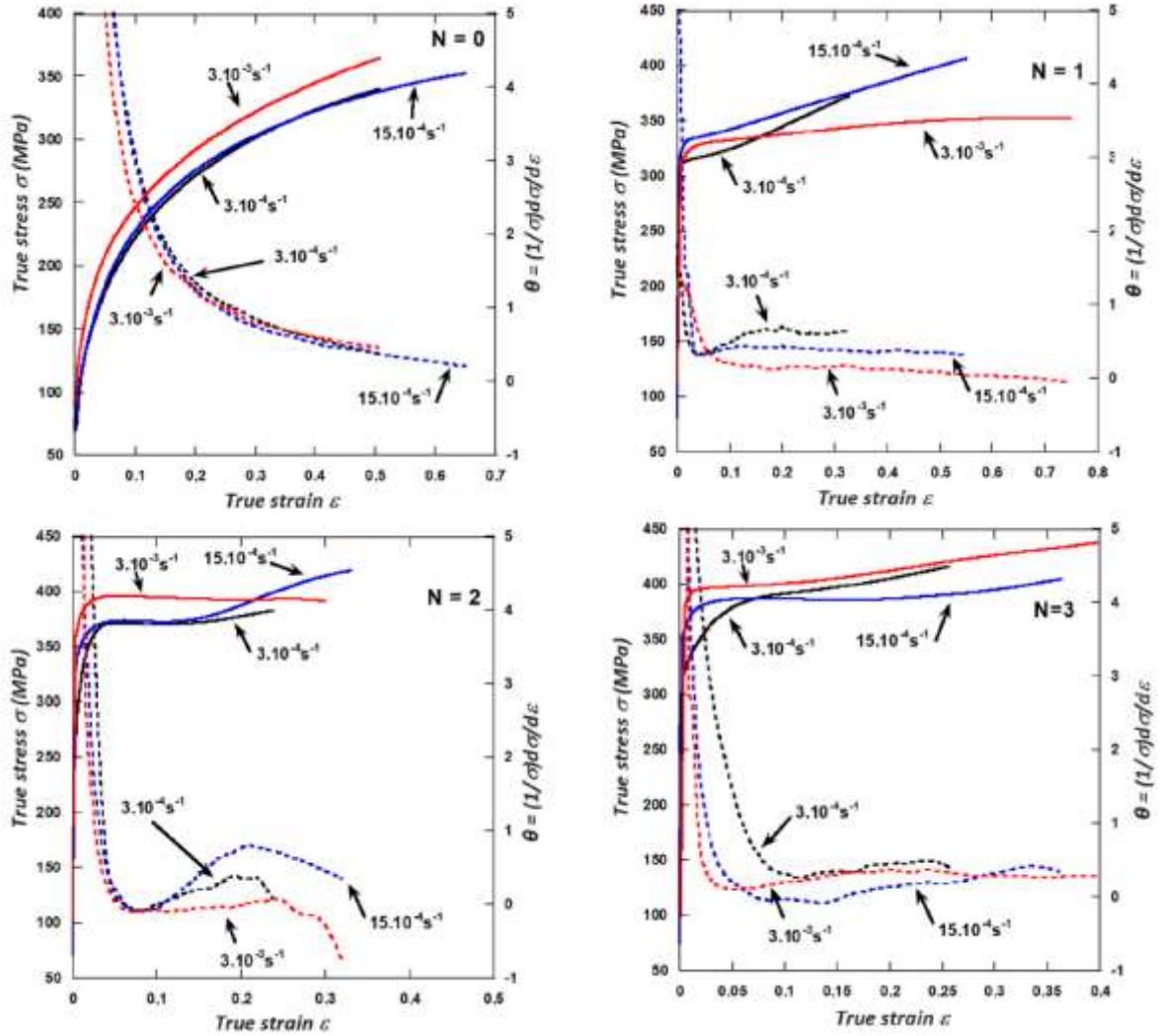
N = 0
N = 1
N = 2
N=3
True stress σ (MPa)
True strain ε
θ = (1/σ)dσ/dε
3.10⁻³s⁻¹
15.10⁻⁴s⁻¹
3.10⁻⁴s⁻¹

Fig.6:

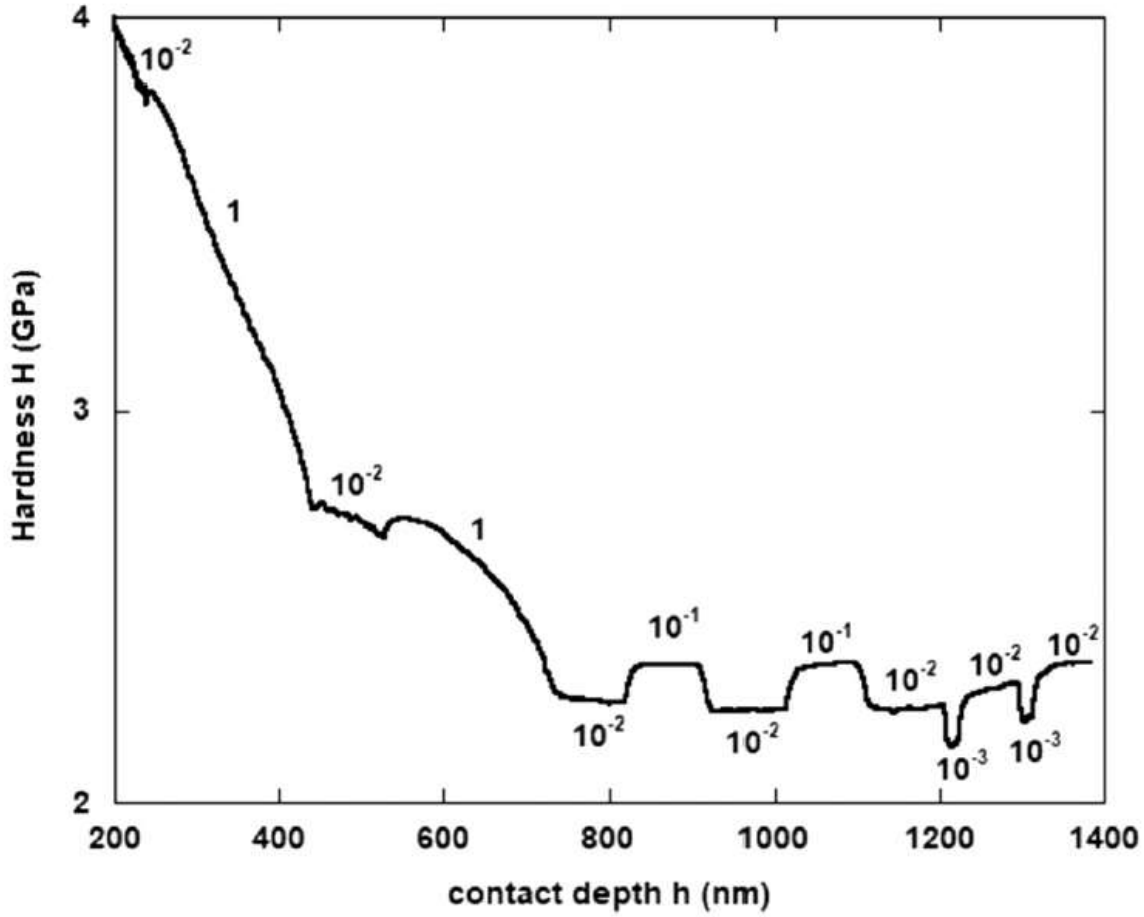
Hardness H (GPa)
contact depth h (nm)
4
3
2
200
400
600
800
1000
1200
1400
10-2
1
10-2
1
10-2
10-1
10-2
10-1
10-2
10-3
10-2
10-3
10-2

Fig. 7:

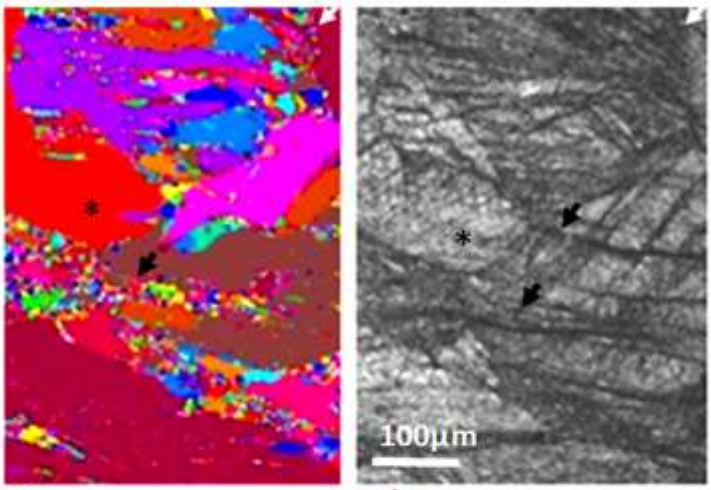

-a- -b-

Fig.8:

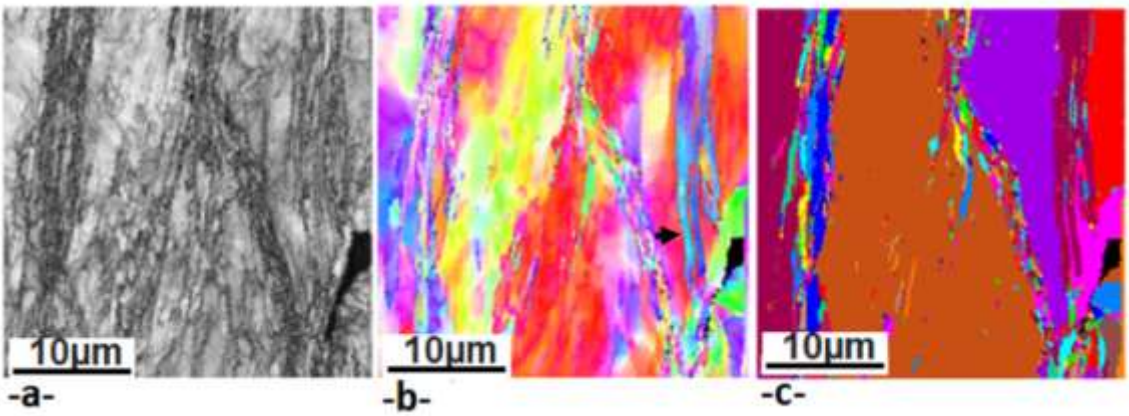

Fig.9:

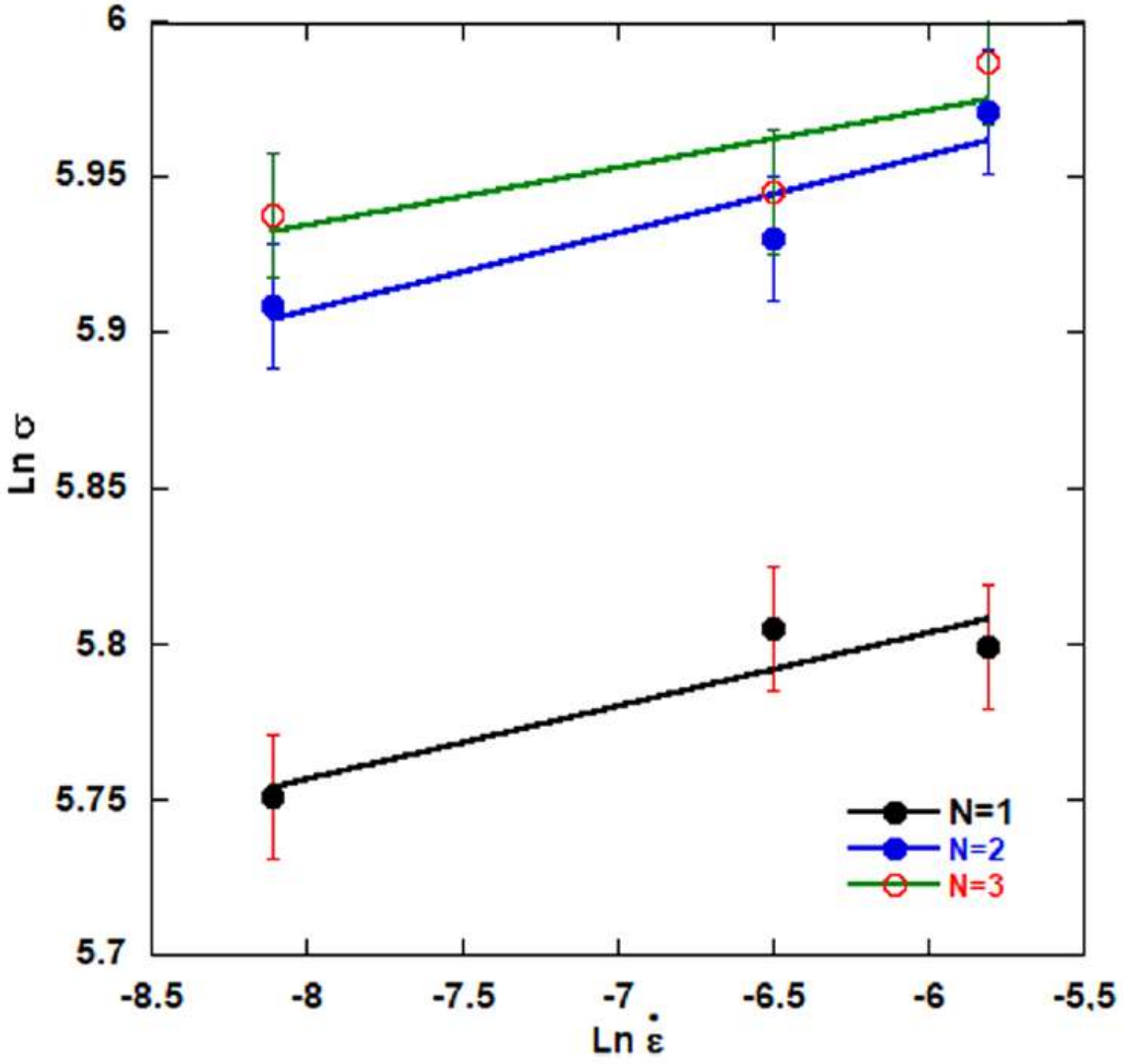

Fig.10:

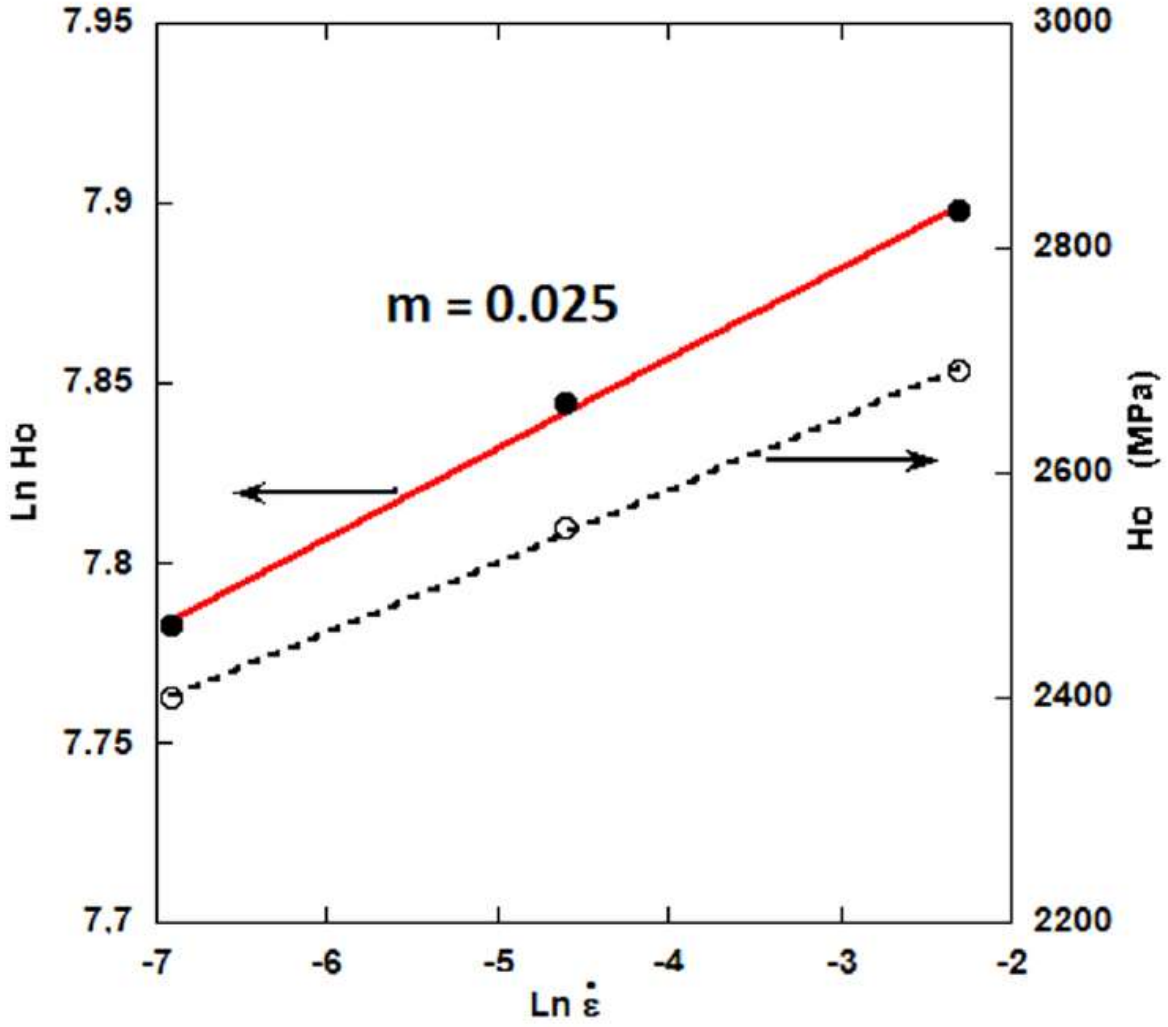
7.95
7.9
7.85
7.8
7.75
7.7
Ln Ho
3000
2800
2600
2400
2200
Ho (MPa)
m = 0.025
-7
-6
-5
-4
-3
-2
Ln ε̇